Chemical Science

ROYAL SOCIETY OF CHEMISTRY

EDGE ARTICLE

View Article Online
View Journal

Cite this: DOI: 10.1039/d5sc09083k

All publication charges for this article have been paid for by the Royal Society of Chemistry

Tunable axial symmetry β-ketoamine covalent organic frameworks for efficient photocatalytic H_2O_2 synthesis in seawater

Jinyang Chen,†[ac] Jie Zhou,†[ab] Na Li,[a] Yeshun Liu,[a] Xubing Deng,[a] Faliang Gou,[a] Zhen Yang,[a] Minfeng Zeng,*[a] Mingchao Shao*[bc] and Yunlong Guo*[c]

Received 20th November 2025
Accepted 20th February 2026

DOI: 10.1039/d5sc09083k

rsc.li/chemical-science

Photocatalytic production of hydrogen peroxide (H_2O_2) from seawater represents a sustainable approach for solar energy conversion. However, complex ionic composition hinders charge transport and accelerates catalyst degradation, undermining efficiency and posing a major challenge to the development of effective photocatalysts. Here, we explore the role of axial symmetry in stabilized β-ketoamine covalent organic frameworks (COFs) for efficient seawater photocatalysis. Three COFs with identical chemical compositions but distinct symmetries, uniaxial (1KtTb), meta-uniaxial (2KtTb), and meta-triaxial (3KtTb), were synthesized. Comprehensive experiments and theoretical analyses reveal that axial symmetry significantly influences light absorption, photocarrier recombination, and the energy barriers of key intermediate pathways (*OOH and *OH). The uniaxial symmetric framework exhibits a narrower bandgap, improved charge separation, and lower reaction barriers, enabling enhanced solar utilization and photocatalytic performance. In real seawater tests from the Zhoushan Sea, the uniaxial symmetric COF achieved record H_2O_2 production rates of 12 865.2 μmol g^{-1} h^{-1} under oxygen and 8557.4 μmol g^{-1} h^{-1} in air, with over 90% activity retained after 20 cycles and 30 days of immersion. Our results demonstrate the application potential of structural symmetry in photocatalysis and guide the design of marine-adapted COFs for efficient H_2O_2 synthesis and photoelectric conversion.

1. Introduction

Hydrogen peroxide (H_2O_2) is a key chemical oxidant and an emerging energy carrier, with rapidly growing demand across industrial disinfection, environmental remediation, and renewable energy storage.[1–3] Conventional industrial production relies primarily on the anthraquinone process, which involves energy-intensive multistep hydrogen and oxygen cycling and generates hazardous byproducts.[4,5] In contrast, photocatalytic synthesis under sunlight using water and oxygen as feedstocks offers a sustainable alternative.[6–9] Seawater, covering over 70% of the Earth's surface and accounting for more than 96% of its water resources, is a highly appealing reaction medium for large-scale photocatalytic H_2O_2 production. However, the presence of a complex ionic matrix such as chloride leads to catalyst degradation and interference with charge separation, posing significant challenges for catalyst stability and efficiency under saline conditions.[10–13] Common photocatalysts such as titanium dioxide and graphitic carbon nitride suffer from narrow spectral response ranges and reduced activity in seawater environments, highlighting the urgent need for stable and efficient materials compatible with real seawater conditions.[14–19]

Covalent organic frameworks (COFs) have emerged as highly promising platforms for photocatalysis, owing to their modular synthesis, extended π-conjugation, high crystallinity, and large specific surface area, which collectively enable efficient light harvesting, charge transport, and catalytic activity.[20–27] Within this broad family, β-ketoamine COFs have recently attracted increasing attention owing to their high crystallinity, chemical tunability, well-ordered π–π stacking, and strong light absorption, along with efficient separation and transport of photogenerated carriers, prompting growing interest in exploring their structural stability and applicability in saline environments.[23,26–30] However, the β-ketoamine linkage (–C=N–C–C=O) is formed through keto-enol tautomerization, a dynamic equilibrium process that is highly sensitive to external stimuli including moisture, ionic strength, and light irradiation.[28–34] Therefore, these frameworks are prone to

[a]Zhejiang Key Laboratory of Alternative Technologies for Fine Chemicals Process, College of Chemistry & Chemical Engineering, Shaoxing University, Shaoxing 312000, P. R. China. E-mail: zengmf@usx.edu.cn

[b]State Key Laboratory of Solid Lubrication, Lanzhou Institute of Chemical Physics, Chinese Academy of Sciences, Lanzhou 730000, P. R. China. E-mail: shaomingchao@licp.cas.cn

[c]Beijing National Laboratory for Molecular Sciences, Organic Solids Laboratory, Institute of Chemistry, Chinese Academy of Sciences, Beijing 100190, P. R. China. E-mail: guoyunlong@iccas.ac.cn

† These authors contributed equally to this work and should be considered co-first authors.

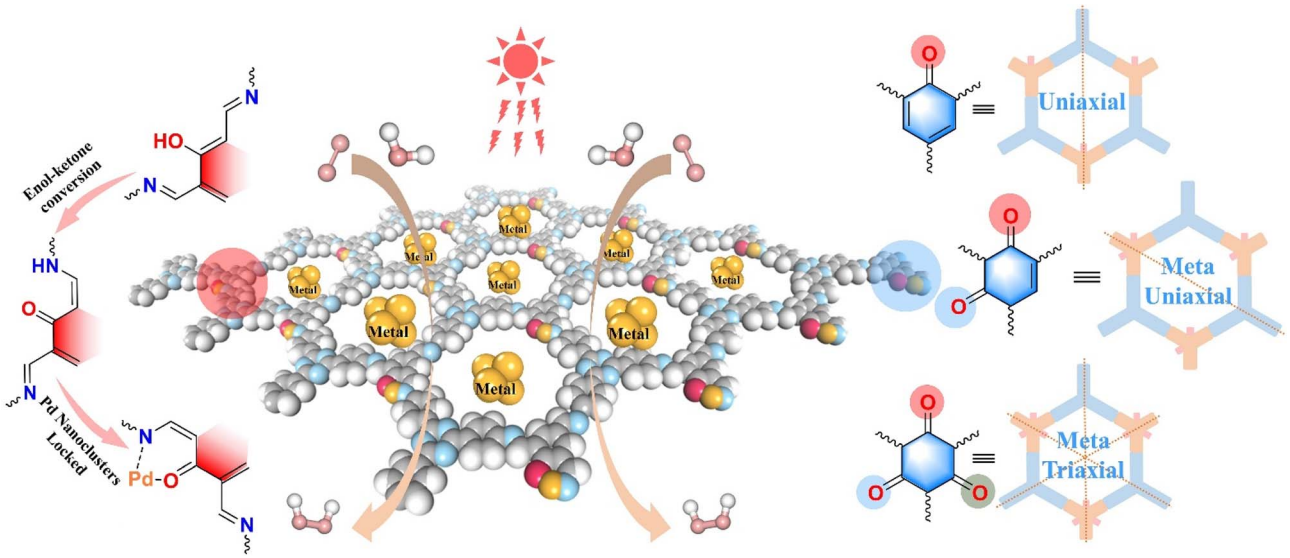

Scheme 1 Schematic diagram of Pd-locked β-ketoamine COFs with different symmetry structures for photocatalytic H_2O_2 production.

structural disorder under saline conditions, ultimately compromising long-term photocatalytic activity.[35] This intrinsic instability complicates the systematic investigation of how topological features, particularly symmetry, affect photocatalytic performance. To address this, a metal coordination strategy was introduced by anchoring palladium nanoparticles

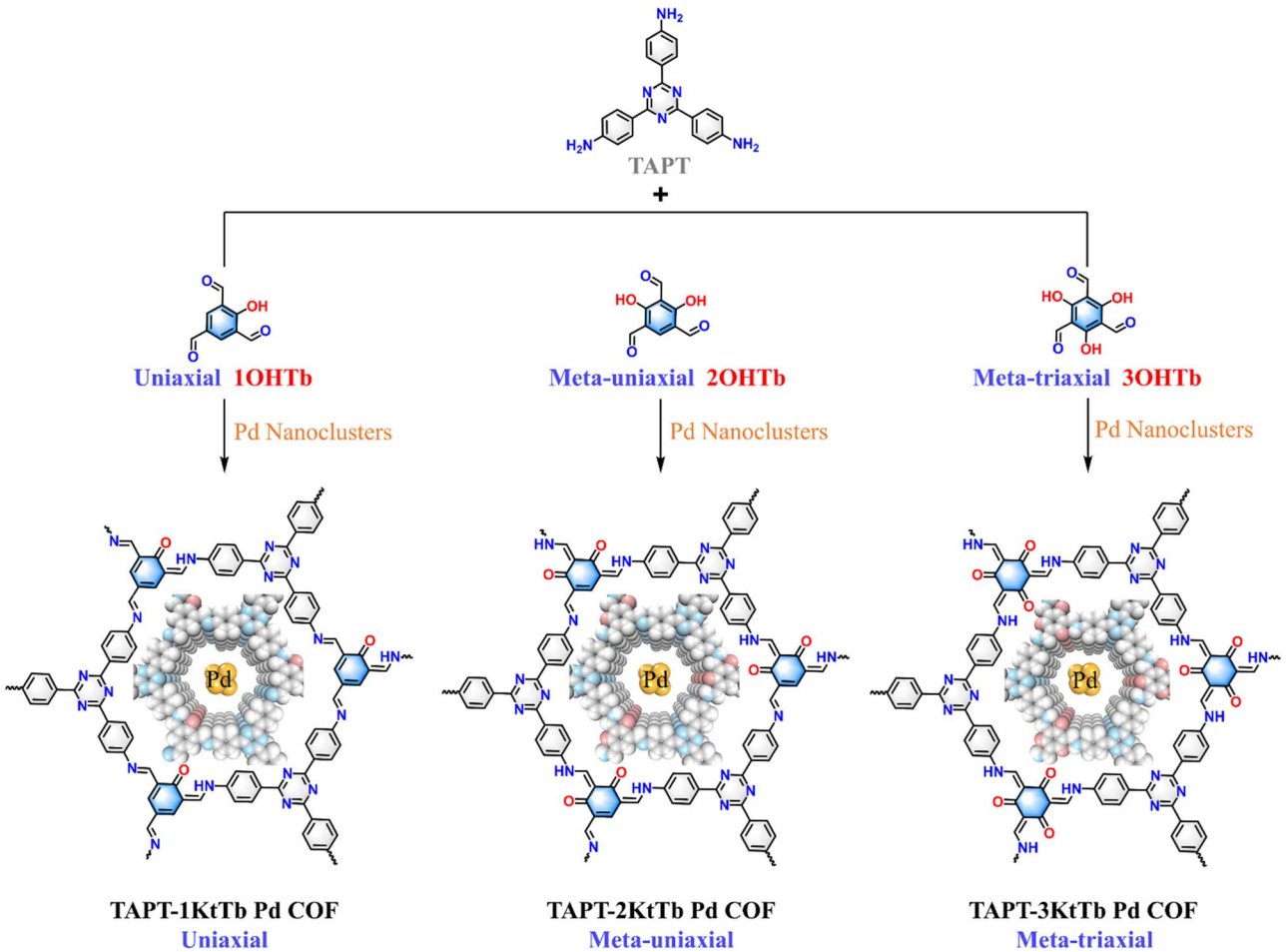

Fig. 1 Schematic diagram of the synthetic route and chemical structures of TAPT-1KtTb Pd COF, TAPT-2KtTb Pd COF, and TAPT-3KtTb Pd COF.

at the nitrogen and oxygen sites within the β-ketoamine backbone in our previous studies. This approach not only stabilizes the tautomeric linkage but also provides well-dispersed active sites that facilitate photogenerated charge separation through a redox cycling mechanism.[36] Despite being effective in improving structural stability and charge dynamics, such modifications inevitably introduce additional variables that mask the intrinsic role of framework symmetry itself, which remains underexplored. Theoretical insights predict that non-centrosymmetric architectures can enable favorable dipole alignment and enhance charge transfer, whereas centrosymmetric frameworks often suffer from dipole cancellation and inefficient carrier separation.[37–40] Nevertheless, direct experimental validation remains scarce, largely due to the synthetic challenge of constructing β-ketoamine COFs that share identical chemical compositions but distinct symmetries. Bridging this gap is essential for disentangling the interplay between structure and function and for advancing the rational design of seawater-compatible, high-efficiency photocatalysts.

In this study, we constructed three β-ketoamine COFs (Scheme 1 and Fig. 1), namely TAPT-1KtTb Pd COF (uniaxial symmetric), TAPT-2KtTb Pd COF (meta-uniaxial symmetric), and TAPT-3KtTb Pd COF (meta-triaxial symmetric), to systematically investigate the influence of topological symmetry on photo-catalytic performance. Among them, the uniaxial symmetric TAPT-1KtTb Pd COF exhibited the most favorable properties, including a narrower bandgap, broader light absorption, extended excited-state lifetime, and the highest photocatalytic activity under both ambient air and real seawater conditions. Notably, the presence of seawater not only provided a practical reaction medium but also highlighted the material's chemical robustness and compatibility with complex ionic environments. Under these conditions, TAPT-1KtTb Pd COF achieved an H_2O_2 production rate of 8557.4 μmol g^{-1} h^{-1}, a quantum efficiency of 10.5%, and a solar-to-chemical energy conversion efficiency of 1.39%. In an oxygen-rich atmosphere, the production rate further increased to 12 865.2 μmol g^{-1} h^{-1}, which ranks among the highest values reported for metal-free photocatalysts. Stability evaluations demonstrated that this COF retained its structural integrity and over 90% of its photocatalytic activity after 20 photocatalytic cycles and up to 30 days of continuous seawater immersion under illumination. Additional experimental and theoretical analyses revealed that the uniaxial symmetric design of β-ketoamine COFs contributes to bandgap narrowing, improved light-harvesting capacity, and enhanced charge transport. Our findings emphasize the potential of symmetry-engineered COFs in the development of efficient and seawater-compatible photocatalysts for H_2O_2 generation, providing valuable insights for the design of future photocatalysts.

2. Materials and methods

2.1. Materials

1,3,5-Tris-(4-aminophenyl) triazine (TAPT), 2-hydroxy-1,3,5-phenyltriformaldehyde (1OHTb), 2,4-dihydroxy-1,3,5-phenyltriformaldehyde (2OHTb), 2,4,6-trihydroxy-1,3,5-phenyltriformaldehyde (3OHTb), palladium chloride, sodium chloride, acetic acid, petroleum ether, tetrahydrofuran, mesitylene, and 1,4-dioxane were obtained from commercial sources and used without further purification.

2.2. Synthesis of TAPT-1KtTb Pd COF

500 mg of 1,3,5-tris-(4-aminophenyl) triazine (TAPT) and 274 mg of 1-hydroxy-1,3,5-phenyltriformaldehyde (1OHTb) were added to a 30 mL Pyrex tube. And then, 12.5 mL of mesitylene and 12.5 mL of 1,4-dioxane were added into the Pyrex tube. The mixture was shaken for 5 minutes and then 0.5 mL acetic acid solution (6 M) was added as a catalyst. The Pyrex tubes were frozen in liquid nitrogen and degassed through three freeze–pump–thaw cycles, then sealed under vacuum. The reaction was carried out at 120 °C for 3 d. After that, the precipitate was filtered and washed with methanol until the filtrate became colorless. The samples were further transferred to a Soxhlet extractor and purified by using tetrahydrofuran as the solvent. Finally, TAPT-1OHTb COF was dried at 120 °C for 12 h.

200 mg of TAPT-1OHTb COFs were first dispersed in 10 mL 0.3% metal Pd precursor solution and stirred at 120 °C for 24 h. Then 20 mL glycol was added to the above solution and stirred at 80 °C for 2 h to reduce Na_2PdCl_4. Finally, the product was centrifuged, washed and dried to obtain the TAPT-1KtTb Pd COF sample. The synthesis of TAPT-2KtTb Pd COF and TAPT-3KtTb Pd COF was similar to that of TAPT-1KtTb Pd COF. It is worth mentioning that ICP data show that the Pd content of TAPT-1KtTb Pd COF, TAPT-2KtTb Pd COF and TAPT-3KtTb Pd COF is 6.6%, 6.7% and 6.5%, respectively, which effectively avoids the difference caused by different Pd content (Table S1).

2.3. Characterization methods

The morphologies of the COF samples were observed using a Zeiss Sigma 300 scanning electron microscope (SEM, Zeiss Group, Germany) and JEM-2100 F high-resolution transmission electron microscope (HRTEM, JEOL Ltd. Japan). The N_2 adsorption/desorption isotherms of the COF samples were collected with a BET surface analyzer of the Micromeritics Tri-Star II 3020 apparatus (Micromeritics Company, USA) at the liquid N_2 temperature of 77 K. Before measurement, all the samples were degassed in a vacuum at 120 °C for 10 h. ^{13}C cross polarization magic angle spinning nuclear magnetic resonance (^{13}C CP/MAS NMR) spectra were recorded on a Bruker Avance III 400 MHz spectrometer. The samples were packed in 4 mm ZrO_2 rotors, which were spun at 8 kHz in a double resonance MAS probe. All spectra were background corrected. The binding energy spectra of C, O, N, and Pd elements of the COF samples were recorded with a Thermo Scientific ESCALAB 250Xi (USA) X-ray photoelectron spectrometer. Pd content within the COF sample was determined using a Leeman ICP-AES Prodigy XP inductively coupled plasma atomic emission spectrometer. The crystal structure of the COF samples was elucidated using an Empyrean X-ray diffraction system (PANalytical company, Netherlands), at a scanning rate of 6° min^{-1} and with 2θ from 2° to 30°. Employing a CHI660e electrochemical workstation, we determined the redox potential of the synthesized photocatalyst

within a conventional three-electrode configuration *via* cyclic voltammetry, and subsequently analyzed the energy level of the highest occupied molecular orbital (HOMO). Their fluorescence spectrum and time-resolved PL decay of the as-made photocatalyst were investigated using a fluorescence spectrometer (F7000) and ultrafast lifetime spectrofluorometer (Delta Flex), respectively. The transition state of the COFs in the photocatalytic system was detected using an INVENIO S *in situ* Fourier transform spectrometer from Bruker, Germany. The formation of reactants, intermediates and products in the reaction system was detected in real time.

2.4. *In situ* electron paramagnetic resonance (EPR) measurements

Superoxide anions of COFs in photocatalytic systems were measured using a Bruker ELEXSYS E500 EPR. Instrument settings were as follows: center field 3511.4 G, sweep width 200.0 G, microwave power 20.00 mW, microwave attenuation 10.0 dB, resonance frequency 9.85 GHz, sweep time 40.0 s, modulation amplitude 1.00 G. By using 5,5-dimethyl-1-pyrrolin-*N*-oxide (DMPO) as a spin trap, the EPR signal formed after the superoxide anion in the sample was captured and showed a specific peak pattern. The absolute quantitative EPR model is used to obtain the number of unpaired electron spins directly through EPR tests. The linear fitting algorithm is used to analyze the linear relationship between the EPR signal intensity and the number of spins in the sample.

2.5. Positron annihilation lifetime spectroscopy (PALS) measurements

The sub-nano level microdefects of the COF sample were measured using an EG&G ORTEC fast-slow system (USA) positron annihilation lifetime spectrometer. ^{22}Na (16 μCi) was used as the positron source and the time resolution of the lifetime spectra was 0.210 ns. A four-component lifetime fitting was conducted for each lifetime spectrum through the Lifetime 9.0 program.

2.6. Density functional theory (DFT) calculations

All calculations were performed in Materials Studio using the hybrid functional chemistry method to account for core-valence electron interactions. The exchange-correlation functional was described within the generalized gradient approximation with the Perdew–Burke–Ernzerhof (PBE) parameterization for calculations. The unit cell used to model the COF photocatalysts contains a repeating unit, which was employed to calculate single-point charges, electron density, and potential distribution, as well as the Gibbs free energy for O_2 reduction and H_2O oxidation reactions. The cutoff energy for geometry optimization and the plane-wave basis set was set at 2×10^{-5} eV and 450 eV, respectively. The convergence criteria for the electronic structure and ensemble relaxation were 2×10^{-5} eV and 0.001 eV Å^{-1}, respectively. Furthermore, the TS-search method was employed to explore the transition states for both the water oxidation reaction (WOR) and oxygen reduction reaction (ORR) pathways, to identify reaction intermediates and to determine the reaction energy barriers.

2.7. Photocatalytic H_2O_2 synthesis

10 mg photocatalyst was dispersed in seawater (50 mL), and placed into the photochemical reaction tank after ultrasonication for 20 min. Pure oxygen was bubbled into the tank before illumination for 30 min. The circulating condensate water system was switched on to maintain the photocatalytic reaction temperature at 298 K. Then, the 300 W Xe lamp was turned on and adjusted to 1.5 G solar intensity (optical power density of $\lambda > 420$ nm, 100 mW cm^{-2}) to irradiate the dispersion.

2.8. H_2O_2 detection methods

In the process of illumination, samples were taken every 20 min, 1.5 mL of reaction liquid was extracted with a needle tube, and the solid–liquid phases were separated with a 0.22 μm filter element. The concentration of H_2O_2 in the extraction solution was determined. Determination of H_2O_2 concentration was conducted by the titanium potassium oxalate color development method. In acidic media, H_2O_2 forms a stable orange complex with titanium ions. The pH = 4, 0.02 M titanium potassium oxalate color developer was configured, and the solution to be tested was mixed with the color developer in a 1 : 1 ratio and allowed to stand for 8 min. The absorbance was measured at 385 nm using a UV/visible spectrophotometer. The linear calibration curve of H_2O_2 concentration (0.2–2.0 mM) was plotted. The linear relationship between H_2O_2 concentration and the absorption intensity was established as follows.

2.9. AQE and SCC calculation

The photocatalytic reaction is carried out in a photochemical reaction chamber, and the photocatalyst (10 mg) and solution (50 mL) are placed in a photoreactor. After ultrasonic dispersion and gas bubbling, the reactor was irradiated with a 300 W Xe lamp (light intensity was 420–700 nm; 100 mW cm^{-2}). Optical power was measured using a CEL-NP2000 optical power meter (Beijing Zhong jiao Jin yuan Technology Co., Ltd., Beijing, China). The photochemical reaction chamber model was CEL-LB70 and the Xenon light source system was CEL-HXF300-T3.

3. Results and discussion

The ordered structures of TAPT-1KtTb Pd COF, TAPT-2KtTb Pd COF, and TAPT-3KtTb Pd COF were determined using powder X-ray diffraction (PXRD). As illustrated in Fig. 2a, diffraction peaks were observed for TAPT-1KtTb Pd COF at 2θ values of approximately 5.4°, 9.8°, 11.3°, 14.6°, and 26.1°, corresponding to the (100), (110), (200), (210), and (001) facets, respectively.[41,42] The experimental PXRD results for TAPT-1KtTb Pd COF closely matched the simulated outcome for the eclipsed AA-stacking mode, with negligible deviation from the predicted pattern (Fig. 2a). The unit cell parameters of TAPT-1OHTb COF were refined to $a = 18.80$ Å, $b = 18.62$ Å, $c = 3.44$ Å, $\alpha = \beta = 90°$, and $\gamma = 120°$ (Fig. S1, SI). Notably, TAPT-2OHTb COF (Fig. 2b) and TAPT-3OHTb COF (Fig. 2c) exhibit similar crystallographic

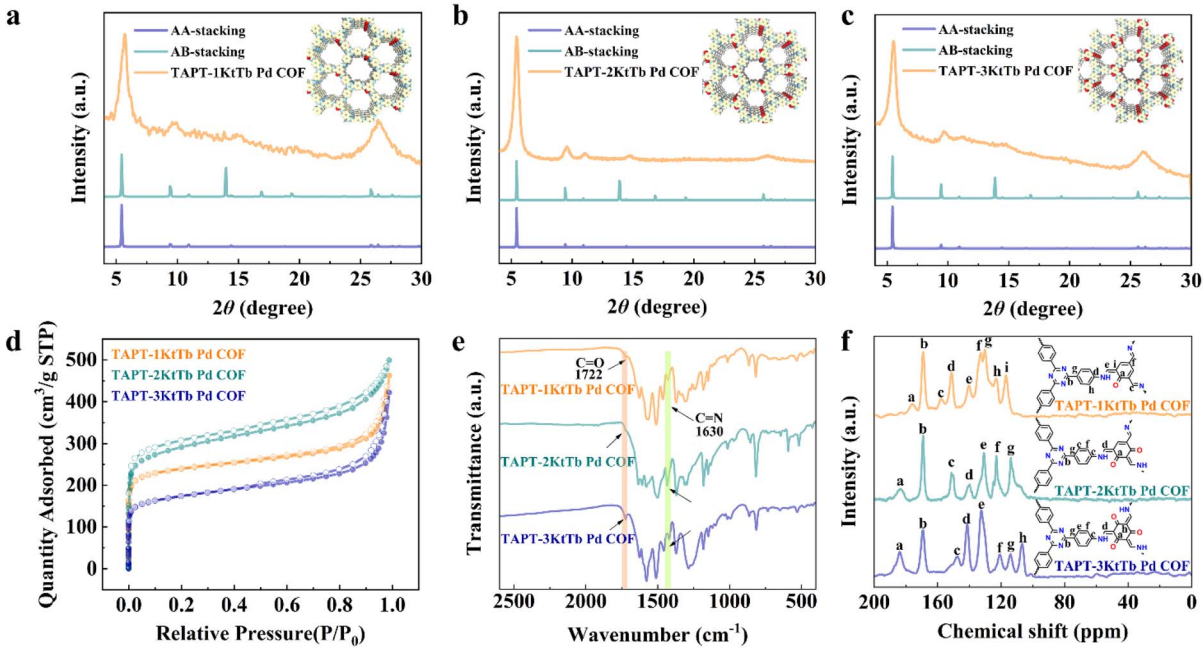

Fig. 2 Crystalline and chemical structures of the three β-ketoamine COFs. (a–c) PXRD patterns of the crystallographic structures. (d) Nitrogen sorption isotherms for characterizing the porosity and surface area. (e) The FT-IR spectrum displaying vibrational absorption bands. (f) The solid-state ^{13}C NMR spectra highlighting the carbon chemical environment.

features, with refined unit cell parameters of $a = 18.70$ Å, $b = 18.67$ Å, $c = 3.45$ Å, $\alpha = \beta = 90°$, $\gamma = 120°$ (Fig. S2), and $a = 18.68$ Å, $b = 18.70$ Å, $c = 3.47$ Å, $\alpha = \beta = 90°$, $\gamma = 120°$ (Fig. S3), respectively. Pawley refinement of the PXRD patterns confirmed the structural consistency, with detailed profiles provided in the SI (Fig. S4 and S5). The porosity and surface areas of TAPT-1KtTb Pd COF, TAPT-2KtTb Pd COF, and TAPT-3KtTb Pd COF were determined using nitrogen adsorption–desorption isotherms at 77 K (Fig. 2d). The Brunauer–Emmett–Teller (BET) method was applied to determine their specific surface areas, which were obtained as 909.8, 1088.1, and 645.1 $m^2\ g^{-1}$, respectively (Fig. S6 and Table S2). The total pore volumes were calculated to be 0.561, 0.681, and 0.504 $cm^3\ g^{-1}$, respectively (Table S2). The nonlocal density functional theory (NLDFT) analysis revealed a pore size distribution of about 0.7 nm for TAPT-1KtTb Pd COF and TAPT-2KtTb Pd COF, while TAPT-3KtTb Pd COF exhibited a main pore size of 1.0 nm (Fig. S7 and Table S2). Notably, although these three COFs have similar molecular structures, they exhibit different symmetries, which create favourable conditions for studying the effect of symmetry on photocatalytic performance.

Scanning electron microscopy (SEM) and high-resolution transmission electron microscopy (HRTEM) results showed the presence of similar interwoven dendritic structures in all three COFs (Fig. S8–S10). To further elucidate the chemical structure, Fourier transform infrared (FT-IR) spectroscopy and solid-state ^{13}C NMR spectroscopy were performed. The FT-IR spectrum (Fig. 2e) displayed vibrational absorption bands at approximately 1722 cm^{-1} and 1630 cm^{-1}, corresponding to the C=O and C=N functional groups, respectively. The solid-state ^{13}C nuclear magnetic resonance spectrum (Fig. 2f) shows distinct local resonances at ~140, 157 and 186 ppm, which are characteristic of the C–N, C=N and C=O bonds. Furthermore, the significant change in the carbon signal confirmed the successful formation of the ketone functionalized structure (Fig. S11). X-ray photoelectron spectroscopy (XPS) was performed to investigate the chemical states and electronic structures of the synthesized COFs (Fig. S12). The C 1s spectra of TAPT-1KtTb Pd COF, TAPT-2KtTb Pd COF, and TAPT-3KtTb Pd COF were deconvoluted into three components at 284.8, 286.7, and 289.8 eV, corresponding to C–C/C=C, C=N–C, and C=O, respectively. Similarly, the N 1s spectra of the three COFs were deconvoluted into peaks at approximately 398.6, 400.7, and 401.2 eV, assigned to C=N, C=N–C, and C–N–C, respectively.[33,43] It is worth mentioning that after the Pd element locks the β-ketoamine bond, the binding energy position of Pd 3d shifts to a low field, showing strong interactions between Pd centers and COFs (Fig. S13).[44] Therefore, all the findings corroborate that COFs have the same β-ketoamine bond, the same elemental composition, and are COFs with different symmetrical structures determined by different quantities and positions of β-ketoamine covalent bonds.

After confirming the structures of TAPT-1KtTb Pd COF, TAPT-2KtTb Pd COF, and TAPT-3KtTb Pd COF, we proceeded to investigate their optical and electrical properties (Fig. S14). The UV-vis diffuse reflectance spectra in Fig. 3a reveal the light absorption characteristics of each COF. Compared to TAPT-2KtTb Pd COF (meta-uniaxial symmetry) and TAPT-3KtTb Pd COF (meta-triaxial symmetry), TAPT-1KtTb Pd COF (uniaxial symmetry) exhibits a pronounced redshift, resulting in a narrower optical bandgap and enhanced redox capacity. These features contribute to its optimized photocatalytic activity. Tauc

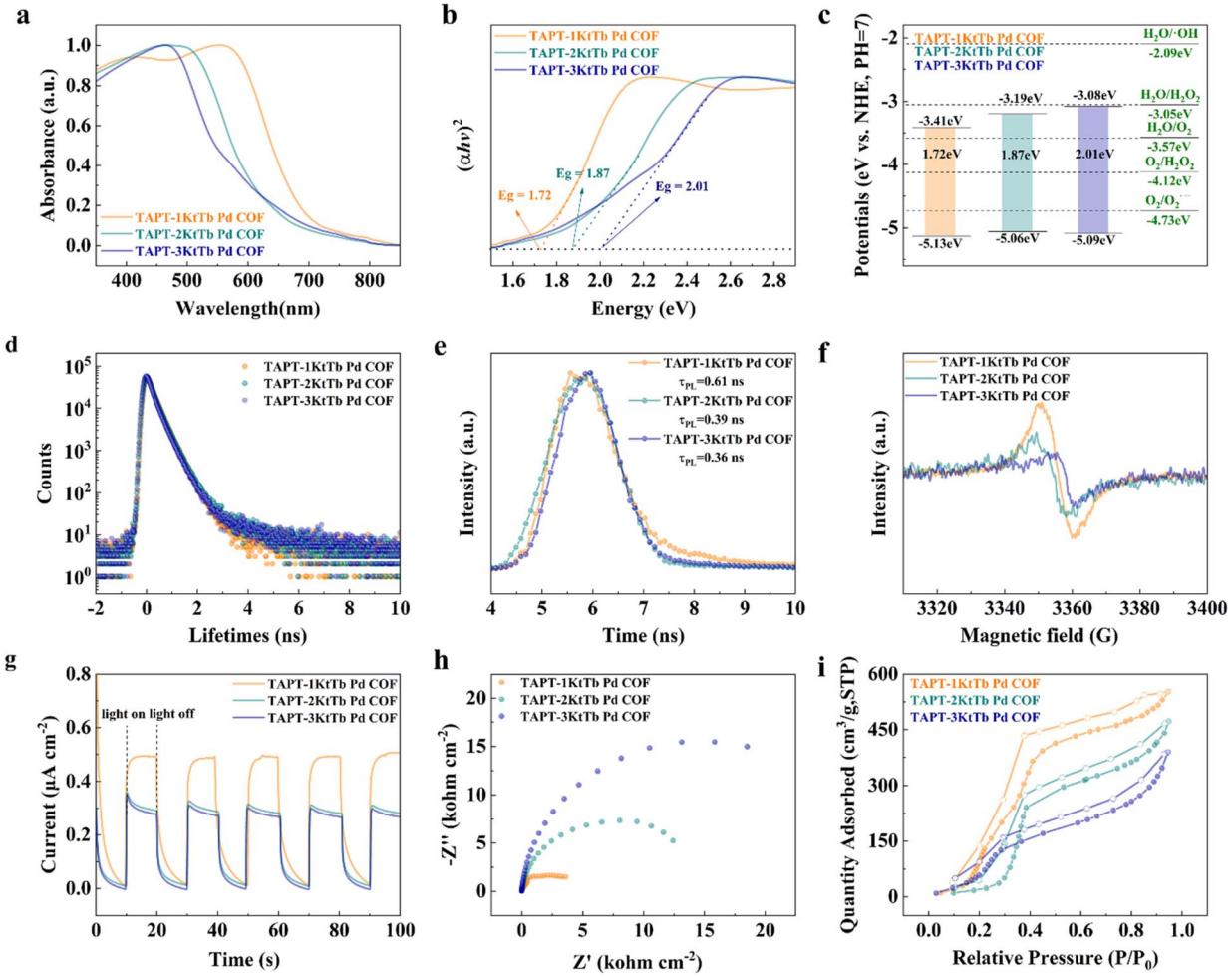

Fig. 3 Optoelectronic properties and hydrophilicity of the three β-ketoamine COFs. (a) UV-vis spectra illustrate the absorption characteristics of the COFs in response to light. (b) Tauc plots provide insights into the bandgap energy distribution. (c) Band structure diagrams reveal the arrangement of electronic energy levels. (d) PALS analysis probes free volume distribution. (e) Time-resolved PL decay curves offer dynamic information about the luminescent characteristics. (f) EPR signals reflect the electronic spin dynamics. (g) Transient photocurrent responses. (h) EIS Nyquist plots. (i) The water vapor adsorption isotherms illustrate the water vapor adsorption capabilities of each COF.

plots in Fig. 3b show that the optical bandgaps of TAPT-1KtTb Pd COF (1.72 eV), TAPT-2KtTb Pd COF (1.87 eV), and TAPT-3KtTb Pd COF (2.01 eV) are all narrower than those of the pristine COF materials (Fig. S15). Moreover, the band positions of the three COFs indicate that H_2O_2 generation *via* the $2e^-$ oxygen reduction reaction (ORR) pathway is thermodynamically feasible (Fig. 3c).[45] To further probe their properties, we employed PALS analysis to detect changes in the long-lifetime component (τ_4) for each COF, as shown in Fig. 3d. A notable decrease in τ_4 was observed after Pd nanocluster immobilization, suggesting that the Pd nanoclusters were effectively distributed within the COF pores (Fig. S16 and Table S3).[46]

Photoluminescence (PL) spectra and time-resolved PL decay curves were analyzed to assess the photo-generated charge separation. As shown in Fig. 3e and S17, TAPT-1KtTb Pd COF exhibited the longest fluorescence lifetime (0.61 ns), compared to 0.39 ns for TAPT-2KtTb Pd COF and 0.36 ns for TAPT-3KtTb Pd COF, indicating that its photogenerated carrier lifetime was longer and the charge separation efficiency was higher.[47] EPR analysis further corroborated these findings, with TAPT-1KtTb Pd COF showing a stronger EPR signal in Fig. 3f and S18, suggesting higher photogenerated electron production efficiency and superior photo-responsive activity, both of which are beneficial for photocatalysis. The photocurrent (*i*–*T*) plots in Fig. 3g demonstrate that the TAPT-1KtTb Pd COF composite exhibits a higher current density, indicating more efficient separation of photogenerated charge carriers. Electrochemical impedance spectroscopy (EIS) analysis, represented in the Nyquist plots in Fig. 3h, reveals a smaller semicircular diameter for TAPT-1KtTb Pd COF, suggesting lower charge transfer resistance and a faster charge transfer rate (Fig. S19).[48] Furthermore, the water vapor adsorption and desorption isotherms in Fig. 3i and S20 show that TAPT-1KtTb Pd COF exhibits a reduced initial adsorption pressure (P/P_0) and enhanced adsorption capacity. These characteristics indicate superior adsorption–desorption performance, which is critical for facilitating the photocatalytic generation of H_2O_2 and

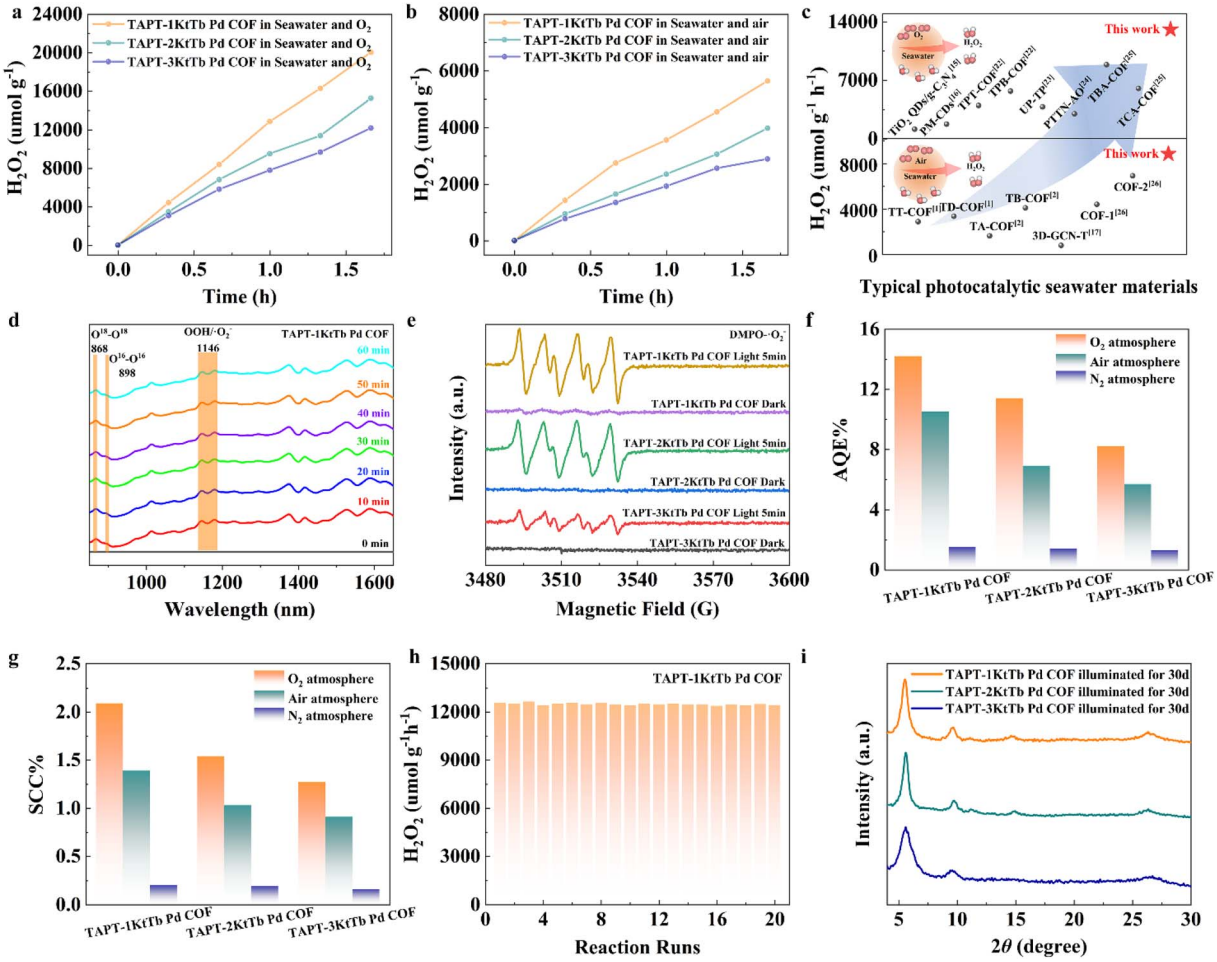

Fig. 4 Photocatalytic activity and durability of the three β-ketoamine COFs. Photocatalytic H_2O_2 production rate in seawater and under (a) air and (b) oxygen. (c) Photocatalytic performance comparison. (d) *In situ* infrared detection of intermediates of TAPT-1KtTb Pd COF. (e) EPR experiments for the COFs using DMPO as the electron-trapping agent. (f) AQE and (g) SCC of each COF. (h) Reuse performance. (i) PXRD patterns after one month of outdoor seawater exposure testing.

enhancing the separation efficiency of H_2O_2 during the water oxidation reaction (WOR) pathway.

The photocatalytic H_2O_2 production activities of TAPT-1KtTb Pd COF, TAPT-2KtTb Pd COF, and TAPT-3KtTb Pd COF were systematically investigated. The corresponding H_2O_2 yields were quantified by colorimetric analysis using potassium titanium oxalate in conjunction with the standard curve (Fig. S21). Under visible irradiation (420–780 nm, 100 mW cm^{-2}), the photocatalytic performance of these COFs was evaluated in seawater under different atmospheric conditions. In air (Fig. 4a), the H_2O_2 production of TAPT-1KtTb Pd COF, TAPT-2KtTb Pd COF, and TAPT-3KtTb Pd COF steadily in-creased over 2 h, reaching average rates of 8557.4, 6351.3, and 5625.2 μmol g^{-1} h^{-1}, respectively. Under an oxygen atmosphere (Fig. 4b), these values further increased to 12 865.2, 9512.5, and 7789.4 μmol g^{-1} h^{-1}. These results represent a significant improvement over most recently reported photocatalysts under comparable conditions (Fig. 4c). Additionally, a control experiment under an N_2 atmosphere (Fig. S22 and S23) confirmed that H_2O_2 production proceeds *via* a dual-channel reaction pathway involving the ORR pathway. Fig. 4d presents the *in situ* Fourier transform infrared (FTIR) spectra of H_2O^{18} isotope labeling experiments, which elucidated the oxygen sources in both pathways. The results indicate that ^{18}O–^{18}O and $\cdot^{18}O_2$ intermediates are generated *via* the $4e^-$ WOR pathway under N_2 and subsequently serve as the oxygen source for H_2O_2.[10,49,50] In addition, *in situ* EPR measurements revealed that the superoxide radical concentration of TAPT-1KtTb Pd COF reaches 1.58×10^{13} mm^3 (spin/cube), which is significantly higher than that of TAPT-2KtTb Pd COF (1.12×10^{13}) and TAPT-3KtTb Pd COF (5.80×10^{12}) (Fig. 4e). *p*-Benzoquinone (BQ), isopropyl alcohol (IPA), and silver nitrate were employed as quenchers for superoxide radicals ($\cdot O_2^-$), hydroxyl radicals ($\cdot$OH), and photogenerated electrons (e^-), respectively (Fig. S24). The results show that the H_2O_2 yield decreased by 68% upon addition of BQ, while no significant change was observed with IPA. Notably, the H_2O_2 yield was nearly completely suppressed upon introduction of silver nitrate. These findings confirm that $\cdot O_2^-$ is the dominant active species, consistent with the *in situ* FTIR and EPR analyses. Together, these results verify that

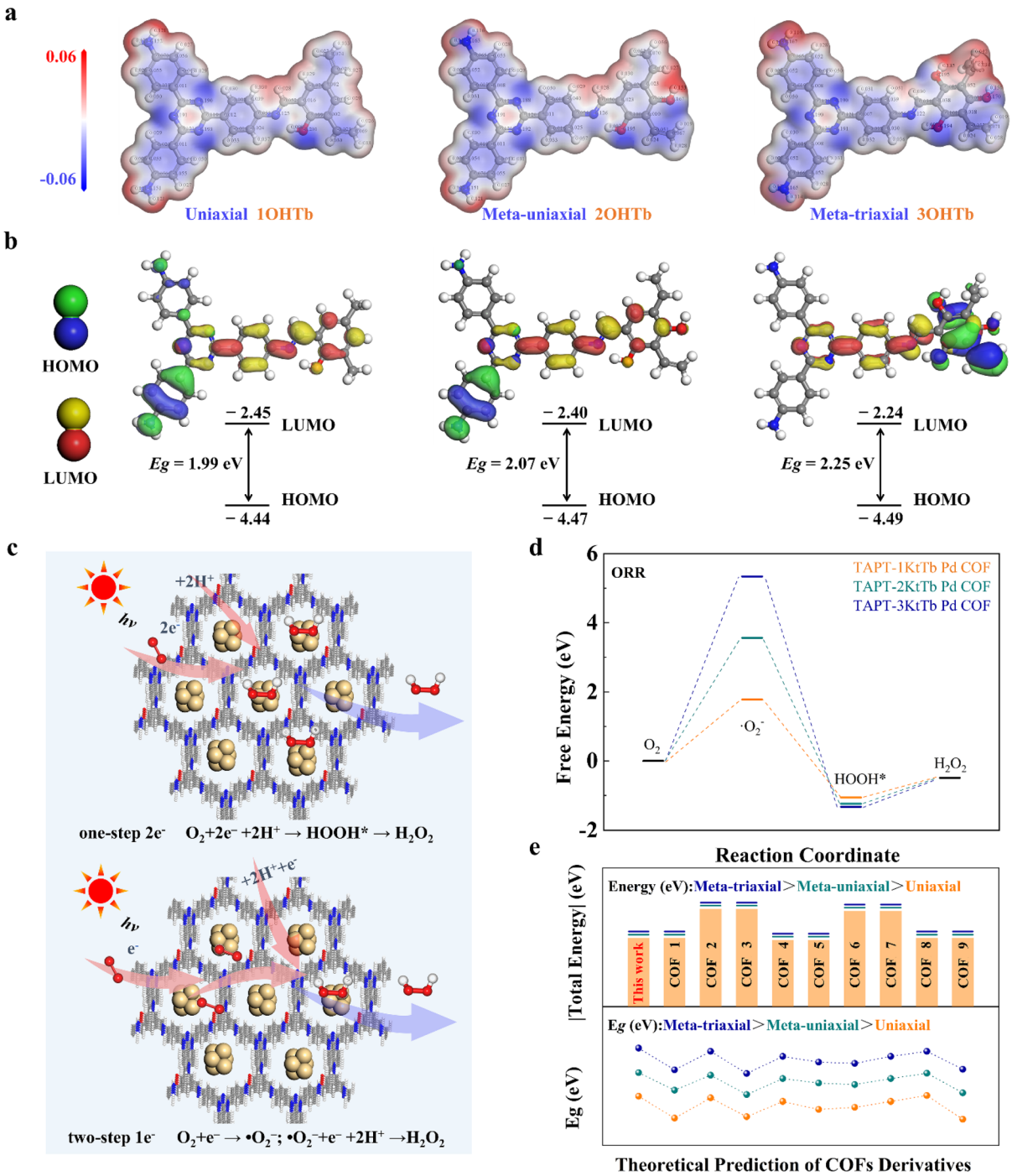

Fig. 5 DFT simulations of the three β-ketoamine COFs. (a) Electron cloud density and electrostatic distribution of the COFs. (b) Frontier molecular orbitals of the COFs are calculated at the PBE level of theory. (c) Diagram illustrating the synthesis of H_2O_2. (d) Gibbs free energy changes of ORR pathways during COF photocatalysis. (e) The variations and governing factors of the charge energy and bandgap in COFs with distinct axial (uniaxial/multiaxial) symmetry.

photocatalytic H_2O_2 production follows both the one-step two-electron pathway ($O_2 + 2e^- + 2H^+ \rightarrow H_2O_2$) and the two-step one-electron pathway ($O_2 + e^- \rightarrow \cdot O_2^-$; $\cdot O_2^- + e^- + 2H^+ \rightarrow H_2O_2$). This significantly enhanced light response further improves the efficiency of photocatalytic H_2O_2 generation (Fig. S25). The apparent quantum efficiency (AQE) and solar-to-chemical energy conversion (SCC) efficiency were measured for the photocatalysts under different atmospheric conditions (Fig. 4f and g). TAPT-1KtTb Pd COF demonstrated the highest AQE of 10.5% (air) and 14.2% (O_2), as well as SCC values of 1.39% (air) and 2.09% (O_2). These results are superior to those of other photocatalysts reported in the literature (Table S4). Overall, TAPT-1KtTb Pd COF with uniaxial symmetry, exhibited the best photocatalytic performance, which aligns with the

characterization findings (Fig. S26). Stability tests were performed over 20 continuous cycles (Fig. 4h), during which the photocatalytic yield remained consistently near 12 000 μmol g^{-1} h^{-1}, indicating excellent photocatalytic stability. Moreover, after one month of outdoor seawater exposure testing, TAPT-1KtTb Pd COF, TAPT-2KtTb Pd COF and TAPT-3KtTb Pd COF still retained excellent crystallinity and specific surface area (Fig. 4i and S27). This stability is attributed to the locking effect of Pd metal.[36]

To elucidate the mechanism of photocatalytic H_2O_2 production, DFT calculations were performed. Computational models of the COFs are shown in Fig. 5a and b. The calculated electron density (Fig. S28) distributions and potential energy profiles indicate that the monoaxially symmetric TAPT-1KtTb Pd COF exhibits lower charge transfer energy compared with its non-monoaxially symmetric counterparts (Fig. 5a and Table S5). Additionally, uniaxially symmetric COFs display narrower bandgaps than meta-uniaxial and meta-triaxial symmetric COFs (Fig. 5b and Table S5), which correlate with broader light absorption and higher solar energy utilization efficiency. These results are consistent with experimental observations of their superior photoelectric properties. To further investigate the reaction mechanism, we simulated the reaction pathway (Fig. 5c) and computed the free adsorption energies at the oxygen reduction and water oxidation sites. TAPT-1KtTb Pd COF exhibits a lower reaction barrier (Fig. 5d) than the other two COFs, suggesting that uniaxial symmetry facilitates both photocatalytic O_2 reduction and H_2O oxidation toward H_2O_2 formation. To validate these observations, we further analyzed the charge potential and frontier molecular orbital (HOMO–LUMO) energy levels for ten representative COFs with different symmetric structures (Fig. 5e and Table S5). The results consistently show that uniaxially symmetric COFs possess lower charge potential energy and more favorable band structures, highlighting their superior photocatalytic performance. Overall, uniaxially symmetric COFs demonstrate distinct advantages in solar energy harvesting and photocatalytic reactivity. These findings provide critical insights into the photocatalytic mechanism and offer guidance for the rational design and optimization of next-generation photocatalytic materials.

4. Conclusions

In summary, we present a symmetry-regulated strategy to enhance photocatalytic H_2O_2 production in real seawater by stabilizing intrinsically labile β-ketoamine COFs through Pd nanocluster coordination. By varying the position and number of substituents on identical building blocks, three structurally analogous but symmetrically distinct COFs, TAPT-1KtTb Pd (uniaxial), TAPT-2KtTb Pd (meta-uniaxial), and TAPT-3KtTb Pd (meta-triaxial), were successfully synthesized. Among them, the uniaxial symmetric TAPT-1KtTb Pd COF exhibited a narrow optical bandgap (1.72 eV), extended light absorption, and a prolonged excited-state lifetime (0.61 ns), collectively enabling efficient charge separation and reduced activation barriers for *OOH/*OH intermediate formation. As a result, TAPT-1KtTb Pd COF achieved outstanding H_2O_2 production rates of 12 865.2 μmol g^{-1} h^{-1} (under oxygen) and 8557.4 μmol g^{-1} h^{-1} (in air) in real seawater samples from the Zhoushan Sea. Notably, high activity was accompanied by excellent long-term stability, with over 90% of its performance retained after 20 cycles and 30 days of continuous seawater immersion under illumination. Theoretical prediction of β-ketoamine COF derivatives indicates that the symmetric structure plays a pivotal role in enhancing carrier separation efficiency, which is crucial for the formation of the *OOH and *OH intermediates in H_2O_2 photocatalysis. This study not only highlights the critical role of topological symmetry in regulating photocatalytic behavior, but also provides a generalizable molecular design paradigm for developing seawater-compatible, high-efficiency COF-based systems for sustainable solar-to-chemical energy conversion.

Author contributions

J. C. and J. Z. contributed equally to this work. J. C., M. Z., M. S., and Y. G. proposed and directed the project. J. C., J. Z., and M. S. designed the entire experimental plan. N. L., Y. L., X. D., and Z. Y. assisted with photocatalytic testing and efficiency characterization. F. G. assisted with cyclic voltammetry testing. J. C., J. Z., and M. S. wrote the paper with help from all authors. All authors commented on the manuscript.

Conflicts of interest

The authors declare no competing financial interests.

Data availability

All data are true and reliable.

The data that support the findings of this study are available in the supplementary information (SI) of this article. Supplementary information is available. See DOI: https://doi.org/10.1039/d5sc09083k.

Acknowledgements

This work was supported by the Zhejiang Provincial Natural Science Foundation (No. LQN25F040012), the National Natural Science Foundation of China (Grant No. 12175149, 12575316, and 11875193), the China Postdoctoral Science Foundation (No. 2024M753284), and the Shaoxing Key Science and Technology Innovation Team Project (No. 2020-34).

Notes and references

1 J.-Y. Yue, L.-P. Song, Y.-F. Fan, Z.-X. Pan, P. Yang, Y. Ma, Q. Xu and B. Tang, *Angew. Chem., Int. Ed.*, 2023, **62**, e202309624.
2 J.-Y. Yue, L.-P. Song, Z.-X. Pan, P. Yang, Y. Ma, Q. Xu and B. Tang, *ACS Catal.*, 2024, **14**, 4728–4737.
3 J.-Y. Yue, J.-X. Luo, Z.-X. Pan, R.-Z. Zhang, P. Yang, Q. Xu and B. Tang, *Angew. Chem., Int. Ed.*, 2024, **63**, e202405763.
4 H. Hou, X. Zeng and X. Zhang, *Angew. Chem., Int. Ed.*, 2020, **59**, 17356–17376.

5 A. Kong, T. Yang, H. Yan, X. Chen, F. Kang, Q. Zhang and R. Liu, *J. Am. Chem. Soc.*, 2025, **24**, 20855–20864.
6 P. V. Kamat, *ACS Energy Lett.*, 2017, **2**, 2157–2158.
7 J. Zhang, F. Xue and Z. Wang, *Angew. Chem., Int. Ed.*, 2025, **64**, e202425617.
8 C. Shu, X. Yang, L. Liu, X. Hu, R. Sun, X. Yang, A. I. Cooper, B. Tan and X. Wang, *Angew. Chem., Int. Ed.*, 2024, **63**, e202403926.
9 L. Wang, C. Han, S. Gao, J.-X. Jiang and Y. Zhang, *ACS Catal.*, 2025, **15**, 5683–5693.
10 M. Kou, Y. Wang, Y. Xu, L. Ye, Y. Huang, B. Jia, H. Li, J. Ren, Y. Deng, J. Chen, Y. Zhou, K. Lei, L. Wang, W. Liu, H. Huang and T. Ma, *Angew. Chem., Int. Ed.*, 2022, **61**, e202200413.
11 C. Shu, P. Xie, X. Yang, X. Yang, H. Gao, B. Tan and X. Wang, *J. Mater. Chem. A*, 2024, **12**, 25927–25933.
12 W. Wang, Q. Song, Q. Luo, L. Li, X. Huo, S. Chen, J. Li, Y. Li, S. Shi, Y. Yuan, X. Du, K. Zhang and N. Wang, *Nat. Commun.*, 2023, **14**, 2493.
13 C. Zhang, P. Shan, Y. Zou, T. Bao, X. Zhang, Z. Li, Y. Wang, G. Wei, C. Liu and C. Yu, *Nat. Sustainable*, 2025, **8**, 542–552.
14 Y. Li, H. Zhou, S. Cai, D. Prabhakaran, W. Niu, A. Large, G. Held, R. A. Taylor, X.-P. Wu and S. C. E. Tsang, *Nat. Catal.*, 2024, **7**, 77–88.
15 W. J. Dong, Y. Xiao, K. R. Yang, Z. Ye, P. Zhou, I. A. Navid, V. S. Batista and Z. Mi, *Nat. Commun.*, 2023, **14**, 179.
16 Q. Wu, J. Cao, X. Wang, Y. Liu, Y. Zhao, H. Wang, Y. Liu, H. Huang, F. Liao, M. Shao and Z. Kang, *Nat. Commun.*, 2021, **12**, 483.
17 R. A. Borges, M. F. Pedrosa, Y. A. Manrique, C. G. Silva, A. M. T. Silva, J. L. Faria and M. J. Sampaio, *Chem. Eng. J.*, 2023, **470**, 144066.
18 H. Zhang, S. Wang, J. Tian and X. Bai, *J. Environ. Chem. Eng.*, 2024, **12**, 112290.
19 S. Zhou, W. Chen, L. Kan, L. Zhu, W. Zhao, D. Wang, Q. Gu, G. Liu, Q. Zhang and P. Gu, *Angew. Chem., Int. Ed.*, 2025, **64**, e202508436.
20 S.-Y. Jiang, Z.-B. Zhou, S.-X. Gan, Y. Lu, C. Liu, Q.-Y. Qi, J. Yao and X. Zhao, *Nat. Commun.*, 2024, **15**, 698.
21 Y. Hou, F. Liu, J. Liang, Z. Li, P. Zhou and M. Tong, *Angew. Chem., Int. Ed.*, 2025, **64**, e202505621.
22 C. Wu, Z. Teng, C. Yang, F. Chen, H. B. Yang, L. Wang, H. Xu, B. Liu, G. Zheng and Q. Han, *Adv. Mater.*, 2022, **34**, 2110266.
23 J.-Y. Yue, L.-P. Song, Z.-X. Pan, M. Cheng, X. Wang, Q. Xu and P. Yang, *Chem. Eng. J.*, 2025, **504**, 158983.
24 X. Shi, Y. You, L. Huang, J. Zhao, W. Ji, L. Li, D. Bu and S. Huang, *Adv. Funct. Mater.*, 2025, **35**, 2414755.
25 Z. Yu, F. Yu, M. Xu, S. Feng, J. Qiu and J. Hua, *Adv. Sci.*, 2025, **12**, 2415194.
26 J.-Y. Yue, Z.-X. Pan, R.-Z. Zhang, Q. Xu, P. Yang and B. Tang, *Adv. Funct. Mater.*, 2025, **35**, 2421514.
27 Y. Xie, F. Mao, Q. Rong, X. Liu, M. Hao, Z. Chen, H. Yang, G. I. N. Waterhouse, S. Ma and X. Wang, *Adv. Funct. Mater.*, 2024, **34**, 2411077.
28 J. Zhang, X. Li, H. Hu, H. Huang, H. Li, X. Sun and T. Ma, *Nat. Commun.*, 2024, **15**, 9576.
29 Y. Yang, X. Chu, H.-Y. Zhang, R. Zhang, Y.-H. Liu, F.-M. Zhang, M. Lu, Z.-D. Yang and Y.-Q. Lan, *Nat. Commun.*, 2023, **14**, 593.
30 L. Zhang, Z. Chen, X.-X. Li, X. Wang, Q. Gu, Z. Zheng, N. Aratani, Y.-Q. Lan and Q. Zheng, *J. Am. Chem. Soc.*, 2025, **31**, 27847–27854.
31 R. Kulkarni, Y. Noda, D. Kumar Barange, Y. S. Kochergin, P. Lyu, B. Balcarova, P. Nachtigall and M. J. Bojdys, *Nat. Commun.*, 2019, **10**, 3228.
32 G.-H. Ning, Z. Chen, Q. Gao, W. Tang, Z. Chen, C. Liu, B. Tian, X. Li and K. P. Loh, *J. Am. Chem. Soc.*, 2017, **139**, 8897–8904.
33 S. Kandambeth, A. Mallick, B. Lukose, M. V. Mane, T. Heine and R. Banerjee, *J. Am. Chem. Soc.*, 2012, **134**, 19524–19527.
34 K. Xiong, Y. Wang, F. Zhang, X. Li and X. Lang, *Appl. Catal., B*, 2023, **322**, 122135.
35 J. Zhang, C. Cheng, L. Guan, H.-L. Jiang and S. Jin, *J. Am. Chem. Soc.*, 2023, **145**, 21974–21982.
36 J. Zhou, J. Chen, N. Li, F. Gou, Z. Yang, M. Zeng and M. Shao, *Small*, 2025, **21**, 2409006.
37 Q. Zhang, X. Zhao, S. Gao, Y. Guo, H. Wang, Z. Liu and J. Wang, *ACS Catal.*, 2025, **15**, 6739–6748.
38 X. Du, H. Ji, Y. Xu, S. Du, Z. Feng, B. Dong, R. Wang and F. Zhang, *Nat. Commun.*, 2025, **16**, 3024.
39 Z. Lin, X. Yu, Z. Zhao, N. Ding, C. Wang, K. Hu, Y. Zhu and J. Guo, *Nat. Commun.*, 2025, **16**, 1940.
40 X. Huang, W. Xie, T. Xu, W. Weng, T. Zhou and J. Guo, *Angew. Chem., Int. Ed.*, 2025, **64**, e202509095.
41 L. Yi, Y. Gao, S. Luo, T. Wang and H. Deng, *J. Am. Chem. Soc.*, 2024, **146**, 19643–19648.
42 Y. Mou, X. Wu, C. Qin, J. Chen, Y. Zhao, L. Jiang, C. Zhang, X. Yuan, E. Huixiang Ang and H. Wang, *Angew. Chem., Int. Ed.*, 2023, **62**, e202309480.
43 W. H. Koppenol, D. M. Stanbury and P. L. Bounds, *Free Radical Biol. Med.*, 2010, **49**, 317–322.
44 C. Zhu, M. Yang, B. Jiang, L. Lu, Q. Fang, Y. Zheng, S. Song, B. Chen and Y. Shen, *Nat. Commun.*, 2025, **16**, 790.
45 J. Han, J. Feng, J. Kang, J.-M. Chen, X.-Y. Du, S.-Y. Ding, L. Liang and W. Wang, *Science*, 2024, **383**, 1014–1019.
46 G. Consolati, D. Nichetti and F. Quasso, *Polymers*, 2023, **15**, 3128.
47 T. Xue, O. A. Syzgantseva, L. Peng, R. Li, Y. Guo, C. Liu, T. Qiao, W. Hao, J. Li, L. Zhu, S. Yang, J. Li and W. L. Queen, *J. Am. Chem. Soc.*, 2024, **146**, 35098–35108.
48 N. Singh, D. Yadav, S. V. Mulay, J. Y. Kim, N.-J. Park and J.-O. Baeg, *ACS Appl. Mater. Interfaces*, 2021, **13**, 14122–14131.
49 Q. Zhu, L. Shi, Z. Li, G. Li and X. Xu, *Angew. Chem., Int. Ed.*, 2024, **63**, e202408041.
50 Y. Luo, B. Zhang, C. Liu, D. Xia, X. Ou, Y. Cai, Y. Zhou, J. Jiang and B. Han, *Angew. Chem., Int. Ed.*, 2023, **62**, e202305355.

